# Supporting Information

## Materials and methods

### 1.1 Chemical Reagents

All chemicals were analytical-reagent grade. Zinc acetate dihydrate ($Zn(CH_3COO)_2 \cdot 2H_2O$, 98 % ~ 101 %) and dimethylimidazole (2-MiM, 99 %) were obtained from Thermo Fisher Scientific (U.S.). Hexadecyl trimethyl ammonium bromide (CTAB, 99 %) was obtained from Macklin (Shanghai, China). Ethyl acetate, hydrochloric acid, and hexane were from Beijing Tongguang Fine Chemical Company (Beijing, China). Titanium(IV) bis(ammonium lactato) dihydroxide (Ti-BALDH, 55 % solution in $H_2O$) and ethanol Sinopharm Chemical Reagent Co., Ltd (Shanghai, China).

### 1.2 Preparation of ZIF-8 and $H_x$ZIF-8

ZIF-8 nanoparticles were prepared via solvothermal synthesis[1] at normal temperature and pressure. Dissolved 0.3 g $Zn(CH_3COO)_2 \cdot 2H_2O$ into 5 mL deionized water, stirring thoroughly until dissolved to prepare the central ion solution. Subsequently, mix 2-MiM with 5 mL 0.54 mmol $L^{-1}$ CTAB solution and stir until fully dissolved. Following this, add 5 mL the central ion solution and stir at 300 rpm for approximately 20 s, during which time the solution transitions from transparent to a milky white appearance. Upon completion of the reaction, centrifuge the mixed solution at 10000 rpm for 10 min to separate the supernatant. The precipitate was then washed once with a 0.25 mg $mL^{-1}$ CTAB solution at 11000 rpm for 10 min. Finally, disperse the washed ZIF-8 nanoparticles uniformly in a 0.25 mg $mL^{-1}$ CTAB solution.

Heat treatment was conducted in an air atmosphere at various temperatures (120,

150, 200, 250, 300, 330, 350, 365, and 400 °C) with a heating rate of 5 °C $min^{-1}$ and maintained for 3 h to obtain $H_x$ZIF-8 (where "*x*" denoted the temperature).

### 1.3 Preparation of $H_{200}$ZIF-8/$TiO_2$

$TiO_2$ was synthesized using the sol-gel method. Initially, 20 mL ethanol and 10 mL Ti-BALDH were added to beaker and stirred at room temperature for 5 min. Subsequently, 4 mL hydrochloric acid and 8 mL ultrapure water were introduced, and stirring continued. The hydrolysis and condensation of tetrabutyl titanate resulted in a sol containing $TiO_2$ nanoparticles. This sol was then dried at 50 °C for 12 h. After drying, the material was ground and calcined in air at a heating rate of 2 °C $min^{-1}$ at 400 °C for 2 h to yield $TiO_2$. The reaction is depicted in Equation (1-3):

$$Ti\left(OC_4H_9\right)_4 + 4H_2O \rightarrow Ti(OH)_4 + 4C_4H_9OH \quad (1)$$

$$Ti(OH)_4 + Ti\left(OC_4H_9\right)_4 \rightarrow 2TiO_2 + 4C_4H_9OH \quad (2)$$

$$Ti(OH)_4 + Ti(OH)_4 \rightarrow 2TiO_2 + 4H_2O \quad (3)$$

$H_{200}$ZIF-8/$TiO_2$ was synthesized using the solid-phase grinding method. The $H_{200}$ZIF-8 and $TiO_2$ powders were placed in a ball milling jar in a specific mass ratio. An appropriate quantity of zirconia balls was added as grinding media. The mixture was ground at 300 rpm for 2 h to ensure thorough mixing and refinement of the powders. Upon completion of the ball milling process, the mixture was removed, the grinding media were separated through sieving, and the powders were collected uniformly, resulting in the formation of the $H_{200}$ZIF-8/$TiO_2$ composite material.

### 1.4 Photocatalytic and photoelectrochemical characterization

The photocatalytic reactor was connected to the circulating condensate water and

photoreduction reaction of TNP was carried under a 300 W Xenon lamp (Zhongjiao Jinyuan Technology Co., Beijing, China). A 3 mL $NaBH_4$ solution was introduced into the reactor containing 40 mL TNP aqueous solution and then the solution transitioned from light yellow to a bright yellow hue. Subsequently, the catalyst was added and 1 mL the sample was collected every minute and analyzed by UV-Vis spectrophotometer (UV-6100, Shanghai Mapada Instruments Co., Ltd., China). The variations in the maximum absorption peak of the solution were recorded and analyzed. The catalytic stability of $H_{200}$ZIF-8/$TiO_2$ was evaluated through cyclic reactions. After the reaction was completed, the photocatalyst was collected via centrifugal filtration and washed repeatedly with water, then dried in a vacuum oven for subsequent catalytic cycles. Additionally, TNT and 2,5-DNP were subjected to catalysis under the same conditions as TNP.

Electrochemical impedance spectroscopy (EIS), transient photocurrent response (TPR), and Mott-Schottky tests were conducted for photoelectrochemical characterization using a standard three-electrode system on the electrochemical workstation. The Mott-Schottky analysis was performed at three frequencies (1000 Hz, 2000 Hz, and 3000 Hz) for each sample. A mixture of Nafion and ethanol (1:50, v:v) was prepared with a 0.5 mol $L^{-1}$ $Na_2SO_4$ solution serving as the electrolyte for electrode preparation. Pt acted as the counter electrode, Ag/AgCl served as the reference electrode, and the sample functioned as the working electrode. Electron paramagnetic resonance (EPR) spectra of hydroxyl radicals (·OH) and superoxide radicals ($\cdot O_2^-$) generated by irradiating the sample with 5,5-dimethyl-1-pyrrolidine-N-

oxide (DMPO) light, as well as the $h^+$ produced by irradiating the sample with 2,2,6,6-tetramethylpiperidin-1-oxide (TEMPO) light, were obtained using an EPR spectrometer. Photoluminescence (PL) spectra and fluorescence lifetime were measured by Edinburgh FLS1000 Fluorescence Spectrometers (Britain).

**1.5 Morphological and structural characterization**

The micromorphology and elemental composition of the ZIF-8 nanoparticles and photocatalyst materials were examined using a Zeiss Supra55 field-emission scanning electron microscope (SEM) from Germany, operating at 10 kV. X-ray diffraction (XRD) analysis was conducted with a Uitima IV Combined multifunctional X-ray Diffractometer from Japan, using a working voltage of 40 kV, a working current of 50 mA, a scanning speed of 5°/s, and a diffraction angle range of 5°~80°. The Fourier transform infrared (FT-IR) spectra were obtained using a Thermo Fisher Scientific Nicolet IS10 FT-IR spectrometer (U.S.). The Brunauer-Emmett-Teller (BET) surface area analyzer (Kubo-X1000, China) was used to identify specific surface area, pore volume, and pore size of the samples. X-ray photoelectron spectroscopy (XPS) was recorded on a Thermo Scientific ESCALAB 250Xi X-ray Photoelectron Spectrometer (U.S.). A JEOL JEM-2100F Field Emission Electron Microscope (Japan) was used to obtain transmission electron microscopy (TEM) and high-resolution TEM (HRTEM) images. The thermal transformation characteristics of ZIF-8 were investigated using Thermogravimetric/derivative thermogravimetric (TG/DTG) and differential scanning calorimetry (DSC) analyses conducted in an air atmosphere over a temperature range of 30 to 1100°C, with a heating rate of 5 $°C \cdot min^{-1}$.

The degradation intermediates of TNP were identified by the LC-MS/MS system (AB SCIEX TripleTOF). Chromatographic separation was implemented using Agilent C18 column (4.6×250 mm, 5μm) with an injection volume of 10 μL and a flow rate of 1 ml $min^{-1}$. The mobile phases were composed of 0.01 mol $L^{-1}$ ammonium formate-formic acid (A) and a solution B methanol. MS fragmentation was carried out in positive electrospray ionization (ESI+) mode with a mass-to-charge ratio (m/z) range from 50 to 1000.

**1.6 Computational details**

Quantum chemical studies are performed using density functional theory (DFT) implemented in GAUSSIAN 16 package[2]. Geometry optimization analysis are calculated at B3LYP hybrid functional[3] with GD3BJ dispersion correlation at 6-311g(d,p) basis sets, Frontier molecular orbital is analyzed by Multiwfn 3.8[4] and VMD v 1.9.3[5] molecular visualization software.

$H_{200}$ZIF-8/$TiO_2$ heterojunction DFT calculations[6, 7] were performed using the Vienna ab initio simulation package (VASP). The generalized gradient approximation (GGA) in the form of Perdew-Burke-Ernzerhof (PBE)[8] was adopted as the exchange correlation functional. The energy cutoff of 450 eV and the k-point meshes of 1×1×1 were proposed to carry out geometry optimization and electronic structure calculation. During the geometry optimization, the entire system is considered to have successfully converged until the convergence thresholds of maximum force and energy were smaller than 0.05 eV/ A and $1.0\times10^{-5}$ eV/atom, respectively. The vacuum slab was set as 15 Å to avoid interactions between neighboring structures.

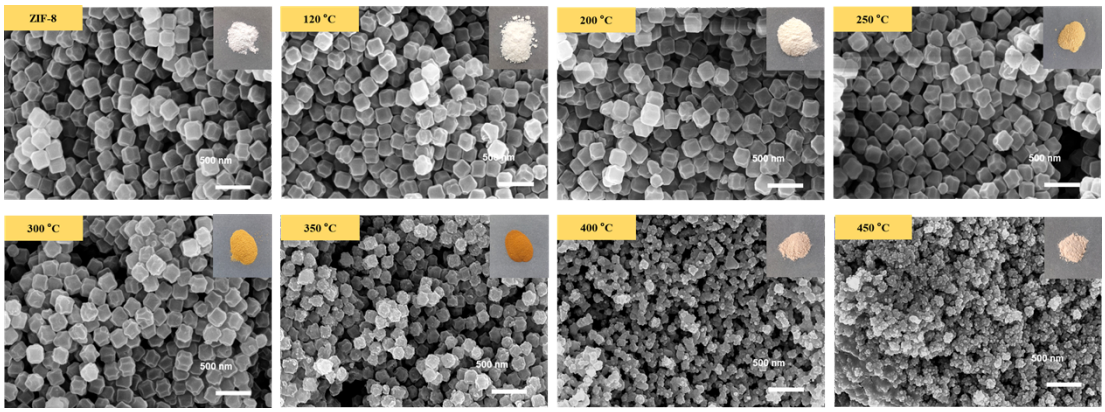


**Figure S1.** SEM and digital images of ZIF-8 and $H_X$ZIF-8.

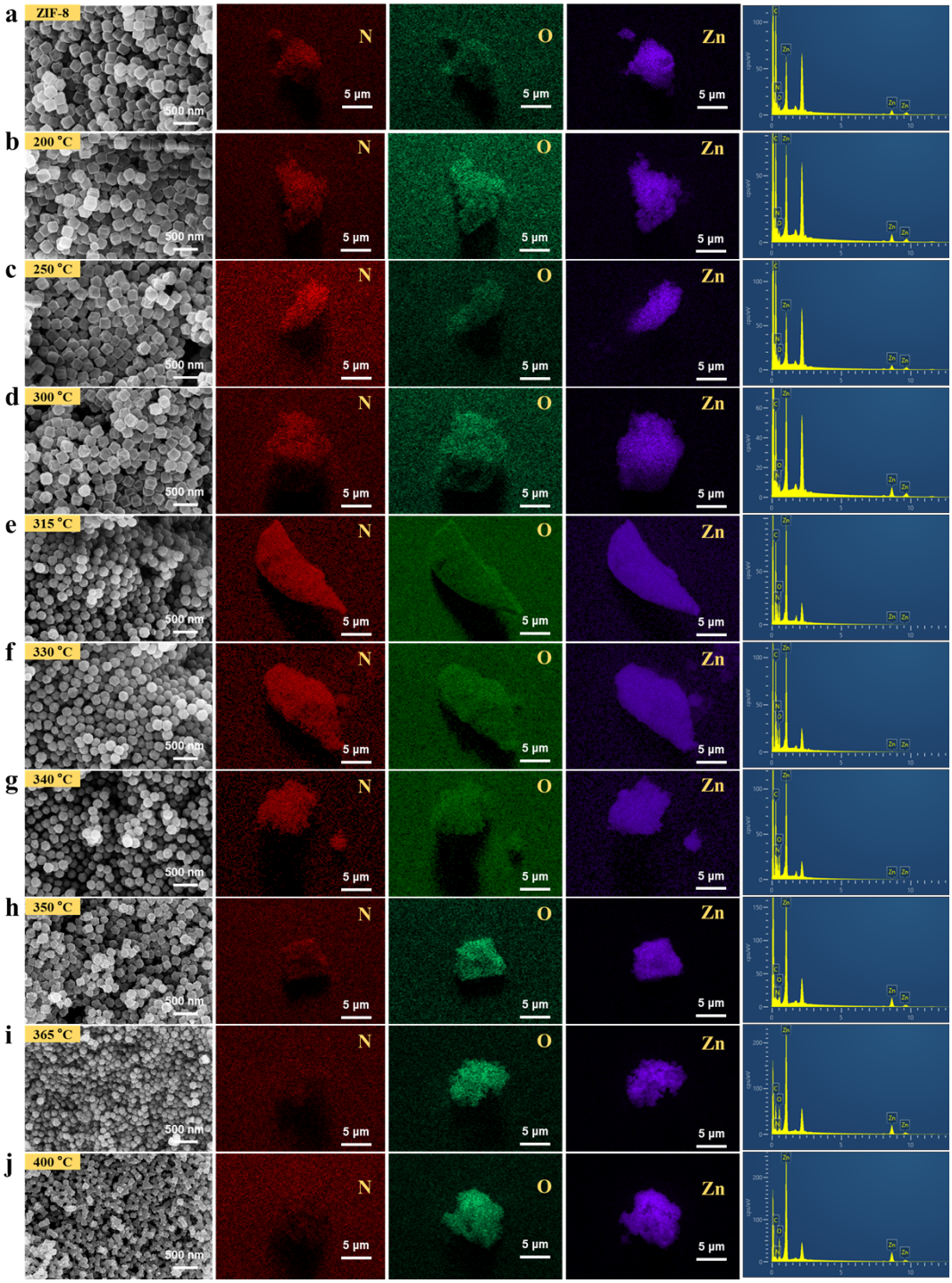


**Figure S2.** SEM images and EDS element mapping results of ZIF-8 at different calcination temperatures (a) ZIF-8, (b) 200°C, (c) 250°C, (d) 300°C, (e) 315°C, (f) 330°C, (g) 340°C, (h) 350°C, (i) 365°C and (j) 400°C.

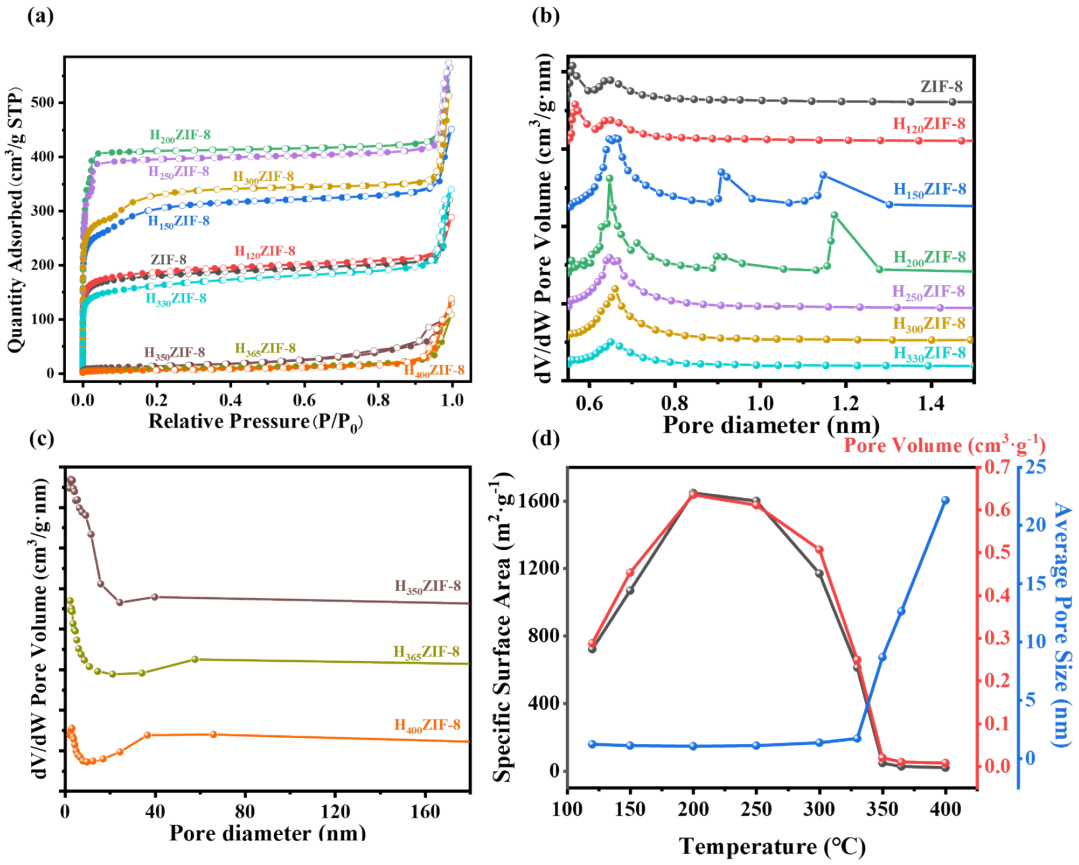


**Figure S3.** (a) $N_2$ adsorption-desorption isotherms, (b-c) pore size distribution profiles of ZIF-8 at different calcination temperatures and (d) variations of specific surface area, pore volume and pore size with different calcination temperatures.


**Figure S4.** Solution color evolution during reduction to reduction.

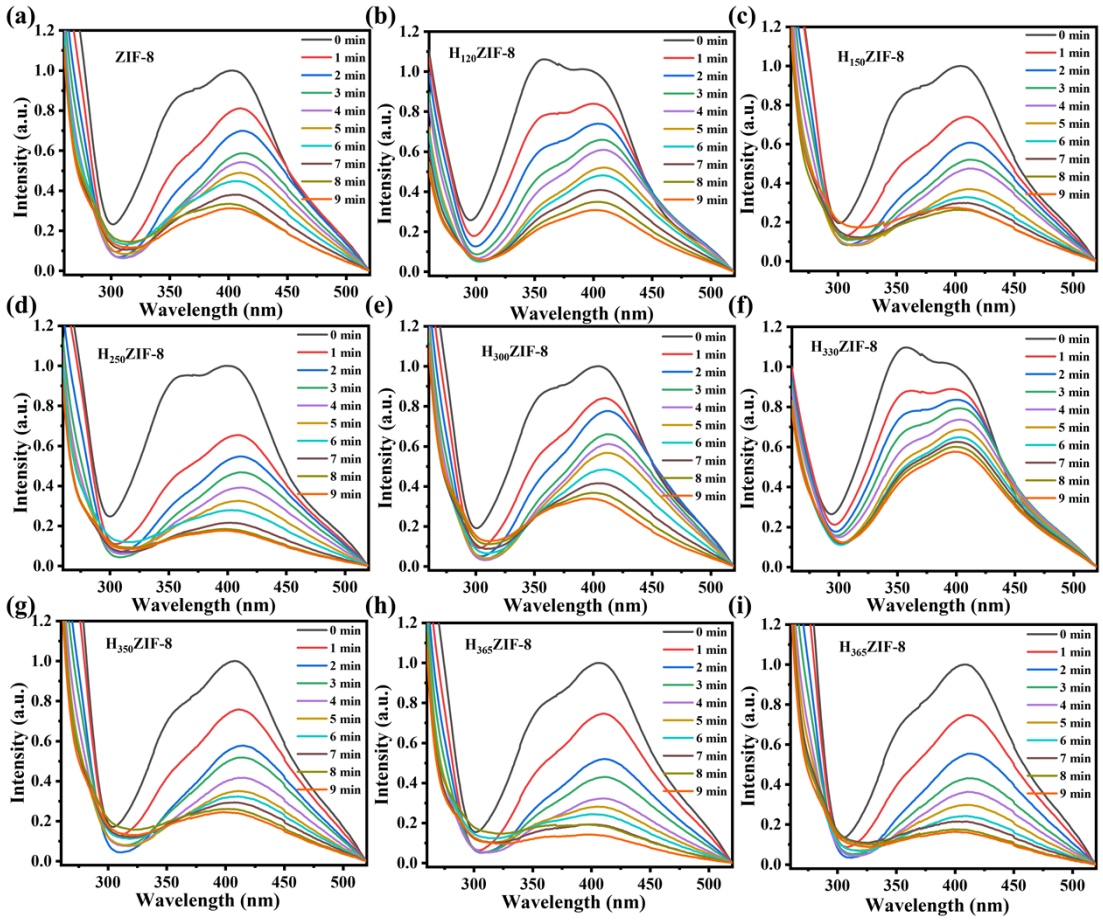


**Figure S5.** UV-vis absorption spectral changes during TNP reduction catalyzed by $H_x$ZIF-8.

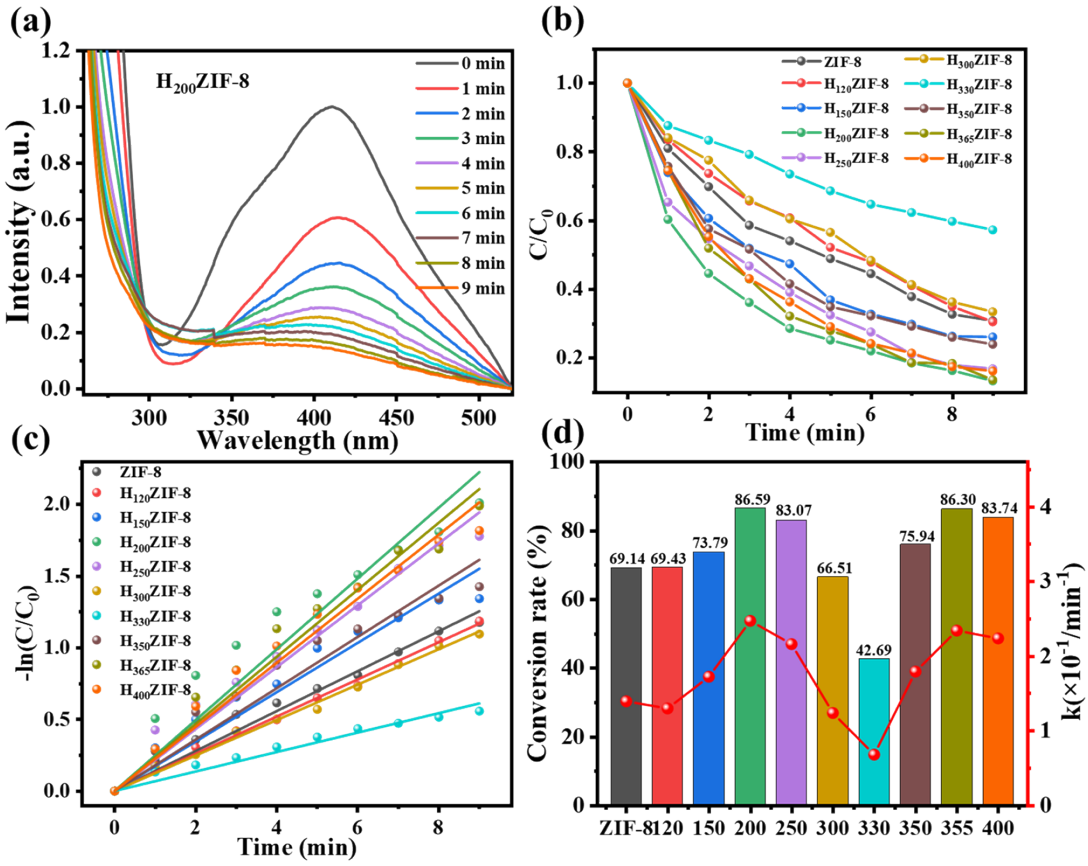


**Figure S6.** (a) UV-Vis absorption spectral changes during TNP reduction catalyzed by $H_{200}$ZIF-8. Under the 300 W xenon lamp, the (b) catalytic reduction rate curve, (c) pseudo-first-order kinetic fitting curve, and (d) k and degradation rate of TNP reduction catalyzed by $H_x$ZIF-8 at different calcination temperatures.

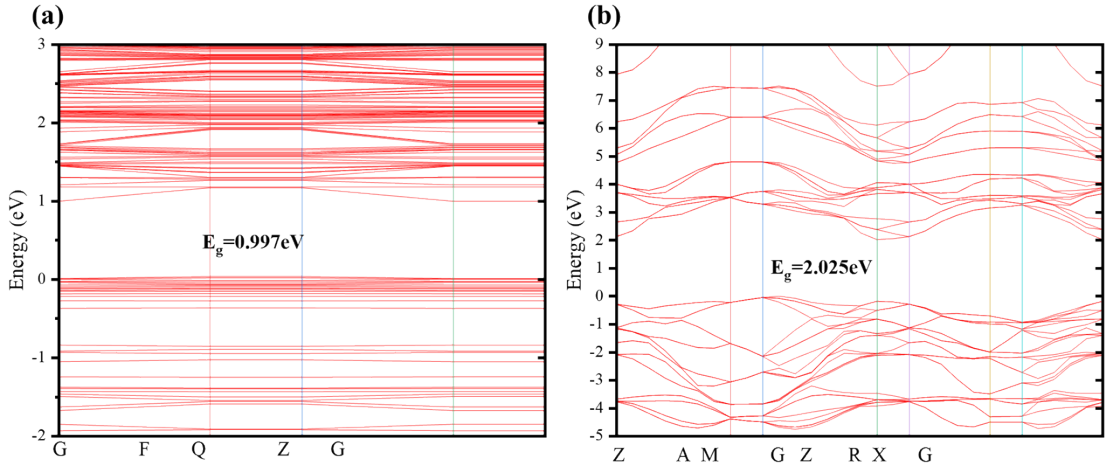


**Figure S7.** Calculated energy band values for (a)$H_{200}$ZIF-8 and (b)$TiO_2$.

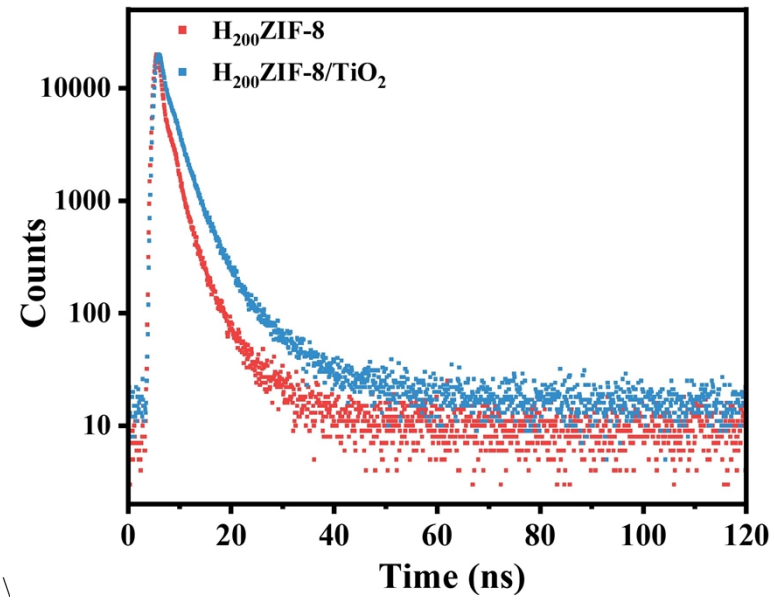


**Figure S8.** Fluorescence decay curves and lifetime of the different catalysts.

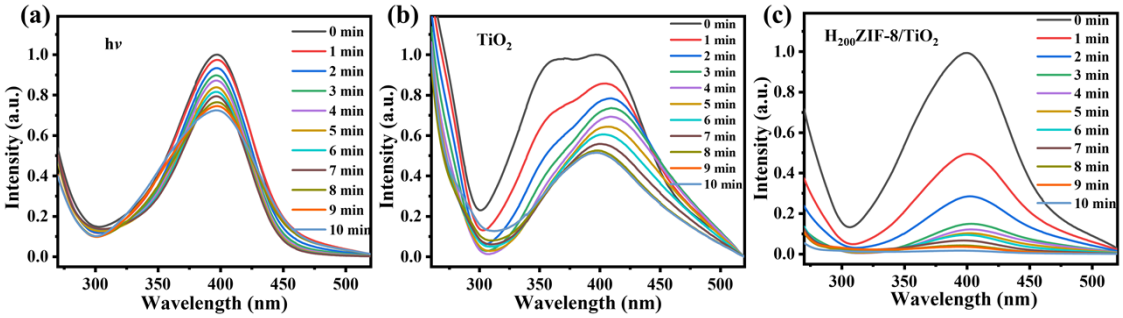


**Figure S9.** UV-vis absorption spectral of TNP measured (a) without catalyst and with (b) pure $TiO_2$ and (c) $H_{200}$ZIF-8/$TiO_2$ as photocatalysts.

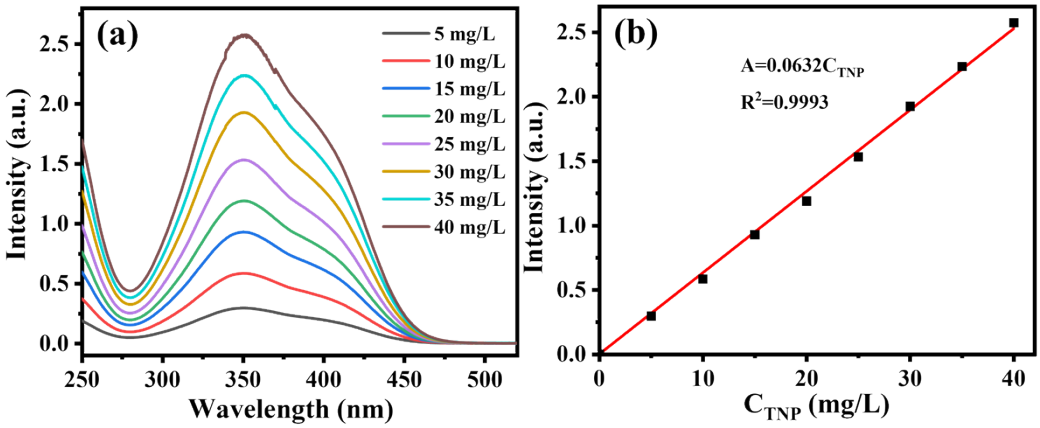


**Figure S10.** UV-vis absorption spectral of TNP with different concentrations. (b) Standard curve of TNP.

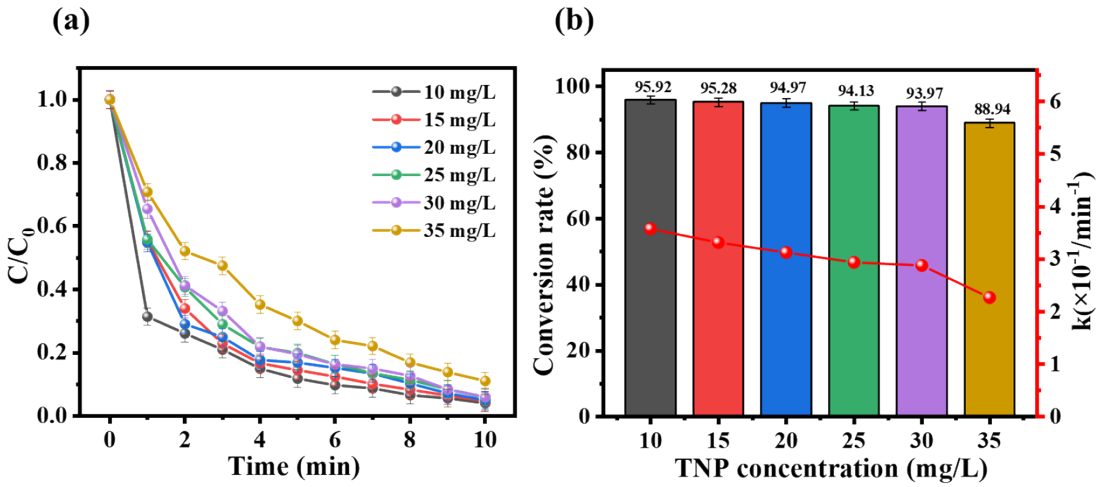


**Figure S11.** The (a) catalytic reduction rate curve and (b) *k* and degradation rate of TNP with the effects of initial TNP concentrations.

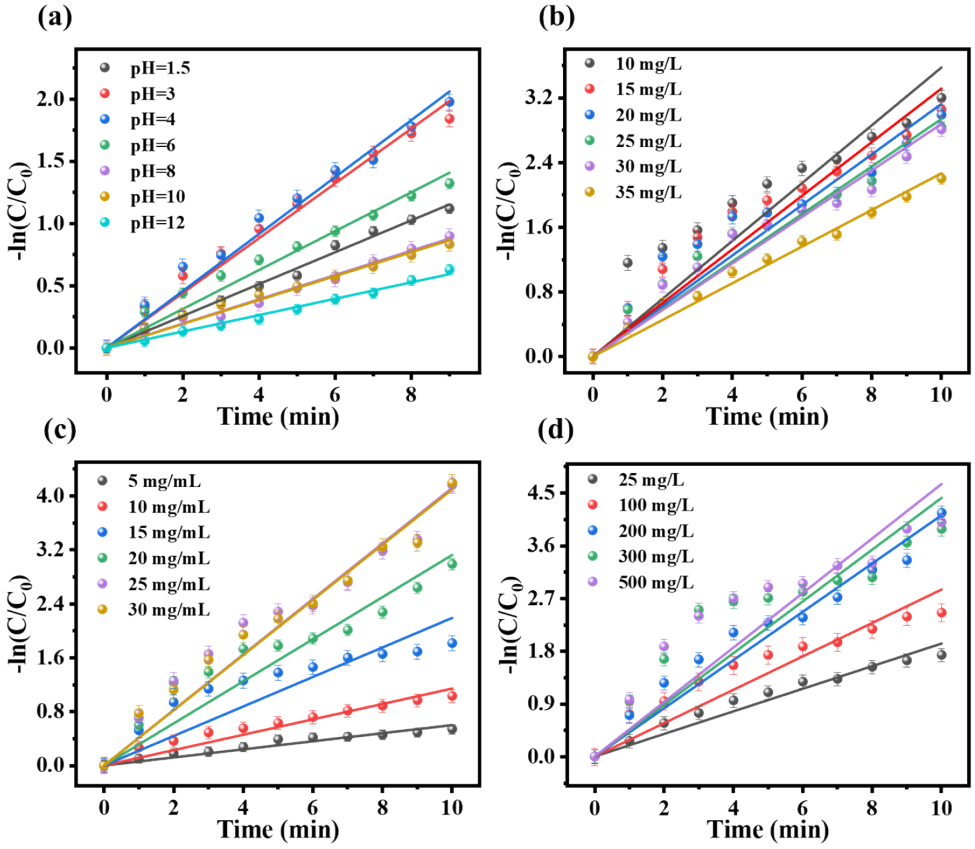


**Figure S12.** The pseudo-first-order kinetic fitting curve of TNP with the effects of (a) initial pH, initial TNP concentrations, (c) $NaBH_4$ concentrations and (d) catalysts dosage.

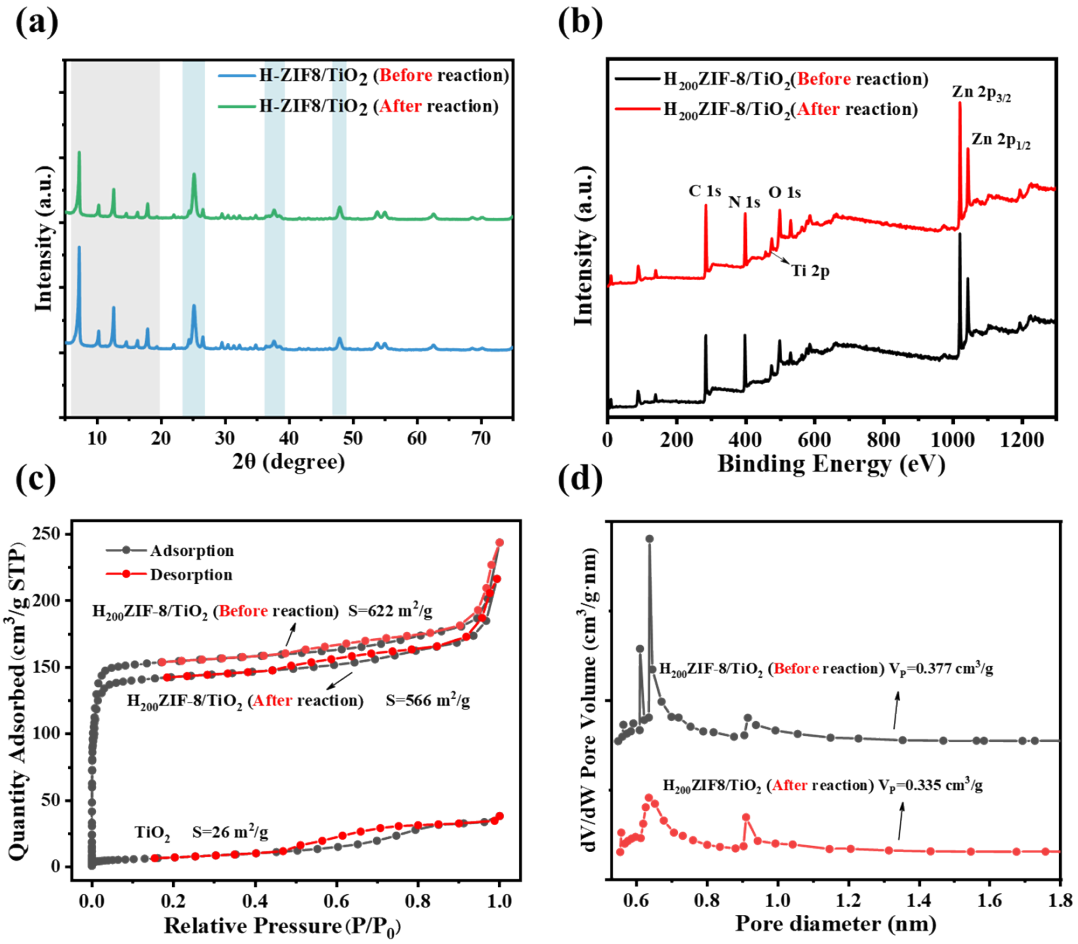


**Figure S13.** (a) XRD, (b) XPS survey spectra, (c) $N_2$ adsorption and desorption isotherms, and (d) pore size distributions of $H_{200}$ZIF-8/$TiO_2$ before and after the photocatalytic reaction.

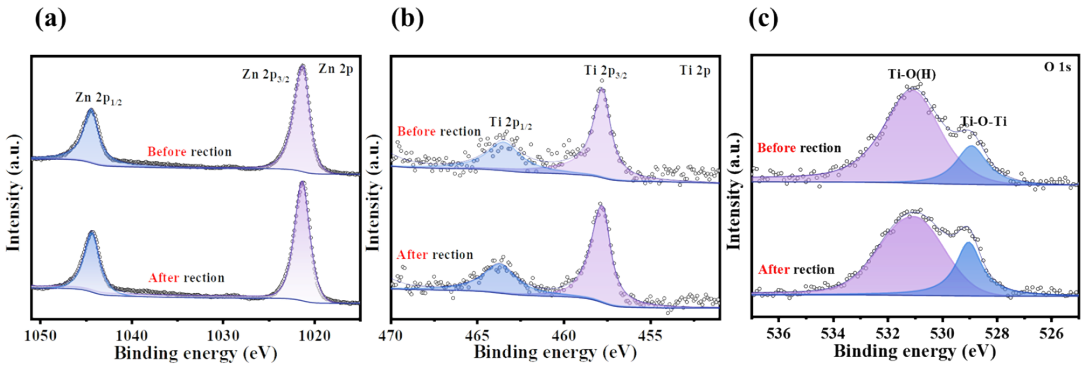


**Figure S14.** High-resolution XPS spectra of (a) Zn 2p, (b) Ti 2p, and (c) O 1s of $H_{200}$ZIF-8/$TiO_2$ before and after photocatalytic reaction.

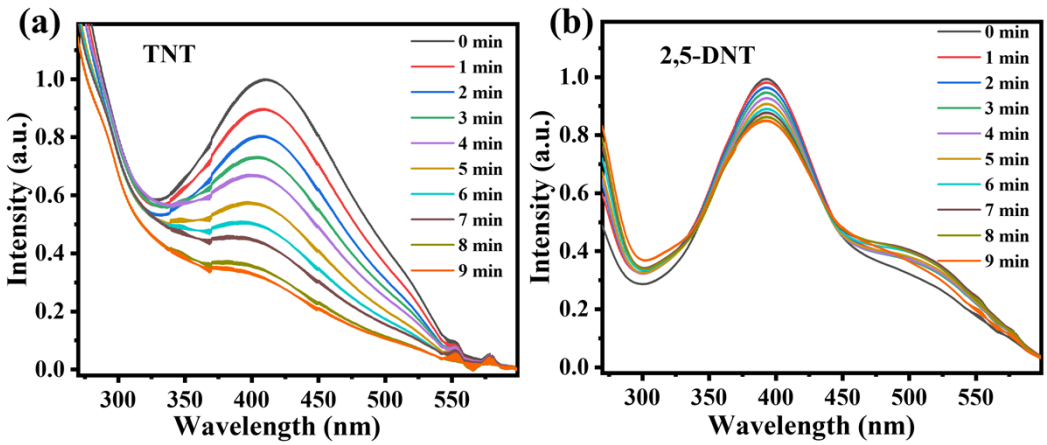


**Figure S15.** UV-vis absorption spectral changes during (a) TNT and (b) 2,5-DNT reduction catalyzed by $H_{200}$ZIF-8/$TiO_2$.

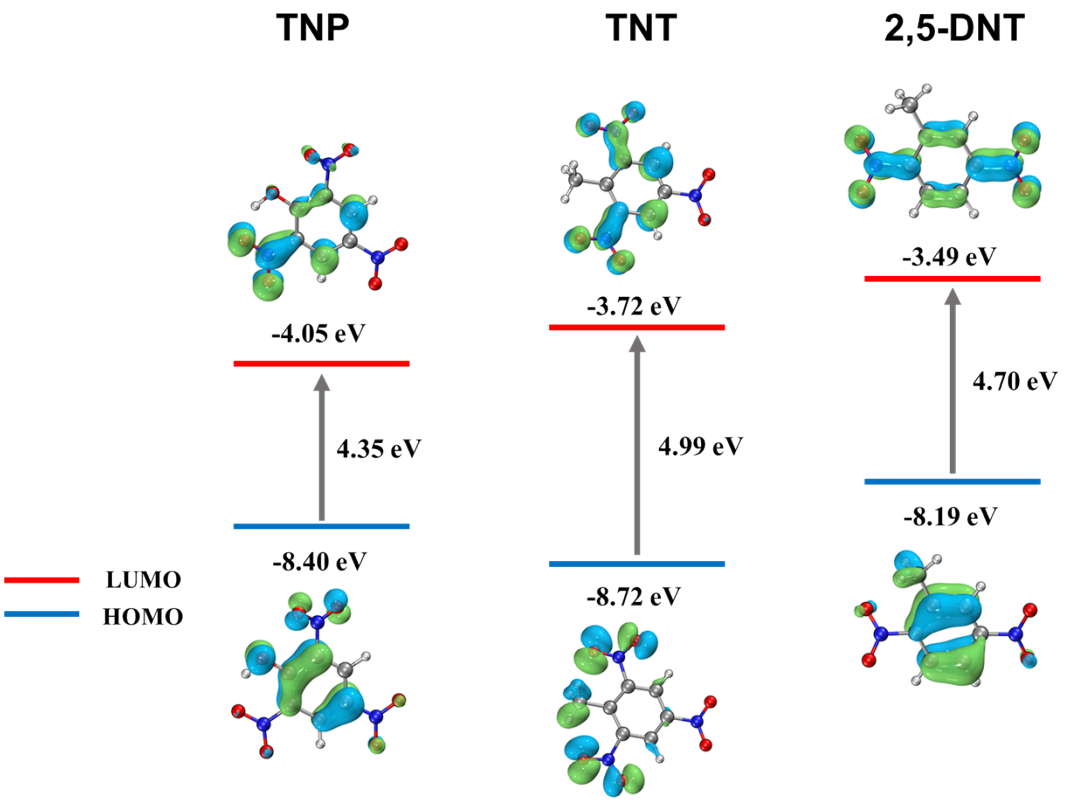


**Figure S16.** HOMO-LUMO energy level profiles of TNP, TNT and 2,5-DNT molecules.

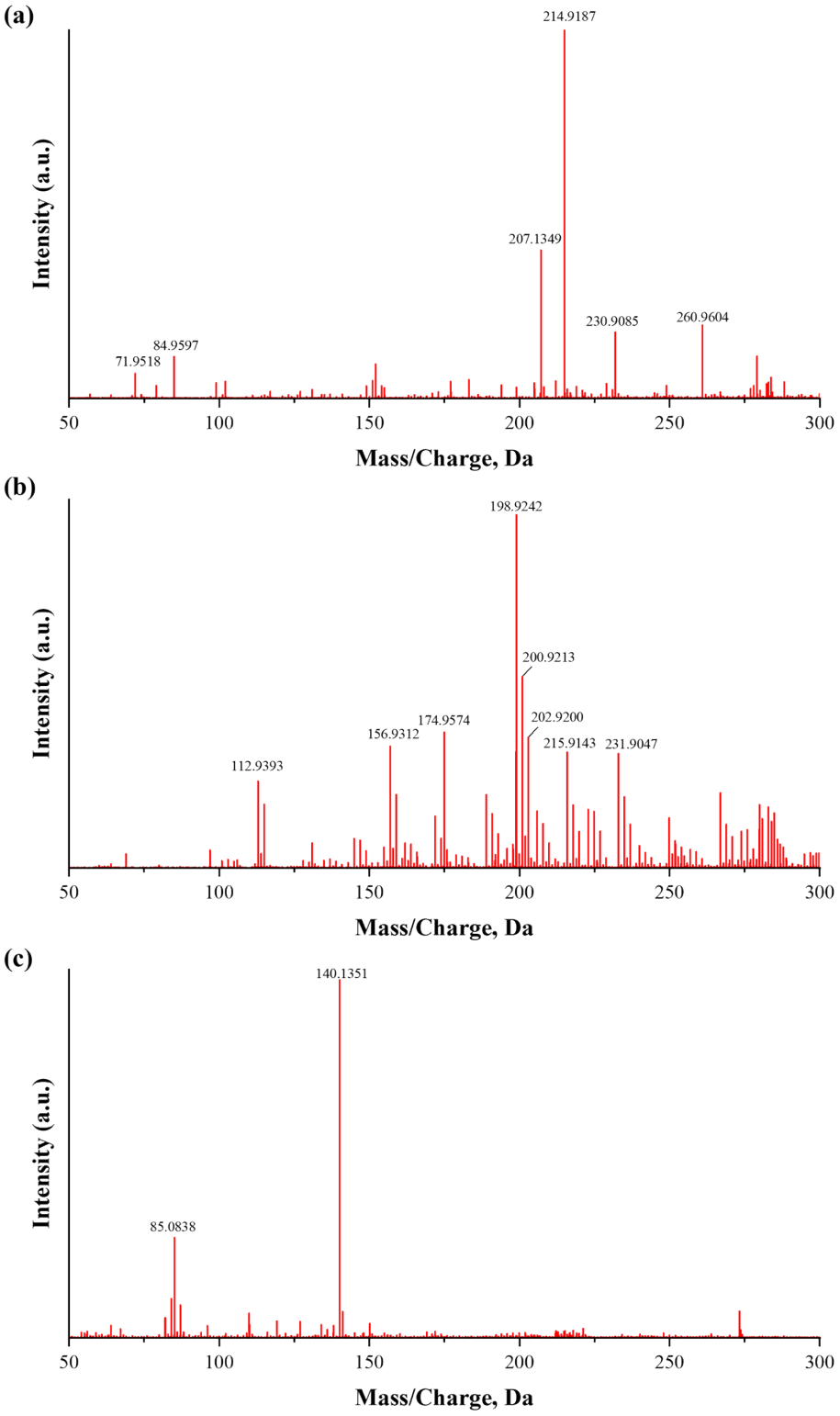


**Figure S17.** Corresponding mass spectra of photodegradation products of TNP.

**Table S1.** Elemental content of ZIF-8 at different calcination temperatures.

| No. | Temperature (°C) | C (Wt%) | N (Wt%) | O (Wt%) | Zn (Wt%) |
|---|---|---|---|---|---|
| 1 | ZIF-8 | 58.07 | 23.12 | 5.09 | 13.72 |
| 2 | 200 | 56.35 | 22.88 | 5.35 | 15.41 |
| 3 | 300 | 49.93 | 20.05 | 6.37 | 23.65 |
| 4 | 400 | 39.88 | 0.00 | 18.43 | 41.69 |

**Table S2.** Pore structure data table of ZIF-8 at different calcination temperatures.

| No. | Temperature (°C) | Specific surface area $S_{BET}$ ($m^2 \cdot g^{-1}$) | Pore volume $V_P$ ($cm^3 \cdot g^{-1}$) | Average pore size $D_P$ (nm) |
|---|---|---|---|---|
| 1 | ZIF-8 | 695 | 0.277 | 1.43 |
| 2 | 120 | 721 | 0.288 | 1.23 |
| 3 | 150 | 1068 | 0.453 | 1.11 |
| 4 | 200 | 1646 | 0.635 | 1.06 |
| 5 | 250 | 1599 | 0.611 | 1.11 |
| 6 | 300 | 1169 | 0.507 | 1.36 |
| 7 | 330 | 612 | 0.249 | 1.72 |
| 8 | 350 | 46 | 0.020 | 8.69 |
| 9 | 365 | 26 | 0.010 | 12.63 |
| 10 | 400 | 19 | 0.008 | 22.15 |

**Table S3.** Pore structure data table of different catalyst

| Sample | $S_{BET}$ ($m^2 \cdot g^{-1}$) | $V_P$ ($cm^3 \cdot g^{-1}$) | $D_P$ (nm) |
|---|---|---|---|
| $TiO_2$ | 26 | 0.059 | 4.52 |
| $H_{200}$ZIF8 | 1646 | 0.635 | 1.06 |
| $H_{200}$ZIF-8/$TiO_2$ (Before reaction) | 622 | 0.377 | 1.21 |
| $H_{200}$ZIF-8/$TiO_2$ (After reaction) | 566 | 0.335 | 1.18 |

**Table S4.** Reduction results of TNP by $H_{200}$ZIF-8/$TiO_2$ under different conditions.

| pH | $C_{TNP}$ (mg/L) | $NaBH_4$ dosage (1mL, mg/mL) | Catalysts dosage (mg/L) | k ($min^{-1}$) | Reduction rate (%) |
|---|---|---|---|---|---|
| 1.5 | 35 | 20 | 200 | 0.1281 | 67.32 |
| 3 | 35 | 20 | 200 | 0.2204 | 84.13 |
| 4 | 35 | 20 | 200 | 0.2266 | 88.94 |
| 6 | 35 | 20 | 200 | 0.1564 | 73.31 |
| 8 | 35 | 20 | 200 | 0.0976 | 59.25 |
| 10 | 35 | 20 | 200 | 0.0961 | 56.51 |
| 12 | 35 | 20 | 200 | 0.0658 | 46.65 |
| 4 | 10 | 20 | 200 | 0.3573 | 95.92 |
| 4 | 15 | 20 | 200 | 0.3314 | 95.28 |
| 4 | 20 | 20 | 200 | 0.3124 | 94.97 |
| 4 | 25 | 20 | 200 | 0.2937 | 94.13 |
| 4 | 30 | 20 | 200 | 0.2877 | 93.97 |
| 4 | 35 | 20 | 200 | 0.2266 | 88.934 |
| 4 | 25 | 5 | 200 | 0.0600 | 41.75 |
| 4 | 25 | 10 | 200 | 0.1142 | 64.36 |
| 4 | 25 | 15 | 200 | 0.2190 | 83.72 |
| 4 | 25 | 20 | 200 | 0.3124 | 94.97 |
| 4 | 25 | 25 | 200 | 0.4120 | 98.44 |
| 4 | 25 | 30 | 200 | 0.4095 | 98.49 |
| 4 | 25 | 25 | 25 | 0.1929 | 82.37 |
| 4 | 25 | 25 | 100 | 0.2851 | 91.43 |
| 4 | 25 | 25 | 200 | 0.4120 | 98.44 |
| 4 | 25 | 25 | 300 | 0.4416 | 97.94 |
| 4 | 25 | 25 | 500 | 0.4653 | 98.17 |

**Table S5.** Comparison of photocatalytic treatment of nitroaromatic compounds by different photocatalysts

| Method | Photocatalysts | Photocatalytic performance | Reference |
|---|---|---|---|
| photocatalytic degradation | $TiO_2$ | RDX(30 mg $L^{-1}$) 80 min complete degradation, HMX (5 mg $L^{-1}$) 20 minutes complete degradation. | [9] |
| photocatalytic degradation | $TiO_2$ | The degradation rates of TNT is 80% after 150 min. | [10] |
| photocatalytic degradation | Zn/MgO nanoparticles | The k is 0.305 $min^{-1}$, and the degradation rate is 45% after 15 min. | [11] |
| photocatalytic degradation | BiOCl nanosheets | The k is 0.107 $min^{-1}$, and it is completely degraded within 90 minutes. | [12] |
| photocatalytic degradation | Polyimine- g-$C_3N_4$/BiOCl | The k is 0.04715 $min^{-1}$, and it is completely degraded after 90 minutes. | [13] |
| photocatalytic reduction | Porous HEA CrMnFeCoNi | The k is 0.17 $min^{-1}$. | [14] |
| photocatalytic reduction | $CeO_2$/Ni-MOF | The k is 0.162 $min^{-1}$ and the degradation rate is 97.6%. | [15] |
| photocatalytic reduction | $H_{200}$ZIF-8/$TiO_2$ | The k is 0.4120 $min^{-1}$, and the degradation rate is 98.44% after 10 minutes. | This work |

## References

[1] C. Avci, I. Imaz, A. Carné-Sánchez, J.A. Pariente, N. Tasios, J. Pérez-Carvajal, M.I. Alonso, A. Blanco, M. Dijkstra, C. López, D. Maspoch, Self-assembly of polyhedral metal–organic framework particles into three-dimensional ordered superstructures, Nature Chem 10 (2018) 78–84.

[2] Frisch, M., Trucks, G., Schlegel, H., Scuseria, G., Robb, M., Cheeseman, J., Scalmani, G., Barone, V., Petersson, G., and Nakatsuji, H. (2016). Gaussian 16, Revision C. 01.

[3] Stephens, P.J., Devlin, F.J., Chabalowski, C.F., and Frisch, M.J. (1994). Ab initio calculation of vibrational absorption and circular dichroism spectra using density functional force fields. The Journal of physical chemistry *98*, 11623-11627.

[4] Lu, T., and Chen, F. (2012). Multiwfn: a multifunctional wavefunction analyzer. Journal of computational chemistry *33*, 580-592.

[5] Humphrey, W., Dalke, A., and Schulten, K. (1996). VMD: visual molecular dynamics. Journal of molecular graphics *14*, 33-38.

[6] P. Hohenberg, W. Kohn, Inhomogeneous Electron Gas, Physical Review 136(3B) (1964) B864-B871.

[7] W. Kohn, L.J. Sham, Self-Consistent Equations Including Exchange and Correlation Effects, Physical Review 140(4A) (1965) A1133-A1138.

[8] J.P. Perdew, K. Burke, M. Ernzerhof, Generalized gradient approximation made simple, PHYSICAL REVIEW LETTERS 77(18) (1996) 3865-3868.

[9] J.-K. Choi, H.-S. Son, T.-S. Kim, M.K. Stenstrom, K.-D. Zoh, Degradation Kinetics and Mechanism of RDX and HMX in TiO2 Photocatalysis, Environmental Technology 27 (2006) 219–232.

[10] H.-S. Son, S.-J. Lee, I.-H. Cho, K.-D. Zoh, Kinetics and mechanism of TNT degradation in TiO2 photocatalysisTiO2, Chemosphere 57 (2004) 309–317.

[11] S. Ali, M.A. Farrukh, M. Khaleeq-ur-Rahman, Photodegradation of 2,4,6-trinitrophenol catalyzed by Zn/MgO nanoparticles prepared in aqueous-organic medium, Korean J. Chem. Eng. 30 (2013) 2100–2107.

[12] J. Yan, B. Jin, P. Zhao, R. Peng, Facile fabrication of BiOCl nanoplates with high exposure {001} facets for efficient photocatalytic degradation of nitro explosives, Inorg. Chem. Front. 8 (2021) 777–786.

[13] J. Yan, X. Song, B. Jin, R. Peng, Construction of novel polyethylenimine-g-C3N4/BiOCl heterojunctions for the efficient photocatalytic degradation of nitro explosives, New J. Chem. 45 (2021) 14655–14664.

[14] H. Peng, Y. Xie, Z. Xie, Y. Wu, W. Zhu, S. Liang, L. Wang, Large-scale and facile synthesis of a porous high-entropy alloy CrMnFeCoNi as an efficient catalyst, J. Mater. Chem. A 8 (2020) 18318–18326.

[15] H. Zhao, X. Pang, Y. Huang, C. Ma, H. Bai, W. Fan, CeO2/Ni-MOF with Synergistic Function of Enrichment and Activation: Efficient Reduction of 4-Nitrophenol Pollutant to 4-Aminophenol, Inorg. Chem. 61 (2022) 19806–19816.